The Astrophysical Journal Supplement Series, 259:45 (13pp), 2022 April https://doi.org/10.3847/1538-4365/ac50b5

Chemical Composition of Bright Stars in the Northern Hemisphere: Star–Planet Connection

G. Tautvaišienė[1], Š. Mikolaitis[1], A. Drazdauskas[1], E. Stonkutė[1], R. Minkevičiūtė[1], E. Pakštienė[1], H. Kjeldsen[1,2], K. Brogaard[1,2], Y. Chorniy[1], C. von Essen[1,2], F. Grundahl[1,2], M. Ambrosch[1], V. Bagdonas[1], A. Sharma[1], and C. Viscasillas Vázquez[1]

[1] Astronomical Observatory, Institute of Theoretical Physics and Astronomy, Vilnius University, Sauletekio av. 3, 10257 Vilnius, Lithuania
grazina.tautvaisiene@tfai.vu.lt
[2] Stellar Astrophysics Centre, Department of Physics and Astronomy, Aarhus University, Ny Munkegade 120, DK-8000 Aarhus C, Denmark
Received 2022 January 7; revised 2022 January 27; accepted 2022 January 29; published 2022 March 25

Abstract

In fulfilling the aims of the planetary and asteroseismic research missions, such as that of the NASA Transiting Exoplanet Survey Satellite (TESS) space telescope, accurate stellar atmospheric parameters and a detailed chemical composition are required as inputs. We have observed high-resolution spectra for all 848 bright ($V < 8$ mag) stars that are cooler than F5 spectral class in the area up to 12 deg surrounding the northern TESS continuous viewing zone and uniformly determined the main atmospheric parameters, ages, orbital parameters, velocity components, and precise abundances of up to 24 chemical species (C(C_2), N(CN), [O I], Na I, Mg I, Al I, Si I, Si II, Ca I, Ca II, Sc I, Sc II, Ti I, Ti II, V I, Cr I, Cr II, Mn I, Fe I, Fe II, Co I, Ni I, Cu I, and Zn I) for 740 slowly rotating stars. The analysis of 25 planet-hosting stars in our sample drove us to the following conclusions: the dwarf stars hosting high-mass planets are more metal rich than those with low-mass planets. We find slightly negative C/O and Mg/Si slopes toward the stars with high-mass planets. All the low-mass planet hosts in our sample show positive Δ[El/Fe] versus condensation temperature slopes, in particular, the star with the largest number of various planets. The high-mass planet hosts have a diversity of slopes, but in more metal-rich, older, and cooler stars, the positive elemental abundance slopes are more common.

Unified Astronomy Thesaurus concepts: High resolution spectroscopy (2096)

Supporting material: machine-readable table

1. Introduction

The NASA Transiting Exoplanet Survey Satellite (TESS) is an ongoing space mission with the primary goal of searching for planets in systems of bright and nearby stars as well as providing precise asteroseismic information (Ricker et al. 2015). The first work of this series (Tautvaišienė et al. 2020; hereafter Paper I) was dedicated to observations of bright stars in the TESS northern continuous viewing zone (CVZ). We observed high-resolution spectra for all stars up to $V < 8$ mag and cooler than F5 spectral type and determined the main atmospheric parameters, ages, kinematic parameters, and abundances of up to 24 chemical elements for 277 slowly rotating stars. In the current work, we extend the homogeneous analysis by observing all 848 stars located around the TESS CVZ up to 12° and increasing the number of bright stars with determined parameters and chemical composition by 740 and the total sample of stars up to 1017. Similar observations and analyses were previously done by us for bright dwarf stars in two preliminary ESA PLATO space mission fields (Mikolaitis et al. 2018, 2019; Stonkutė et al. 2020). As the number of bright stars with confirmed planets in the covered sky areas has already increased up to 25, we decided to address several questions about the star–planet connection that are currently under discussion in the literature: the stellar chemical composition and planet mass relation (e.g., Santos et al. 2017; Suárez-Andrés et al. 2017, 2018; Bedell et al. 2018; Hinkel & Unterborn 2018; Adibekyan 2019; Cridland et al. 2019; Bashi & Zucker 2021; Delgado Mena et al. 2021; Kolecki & Wang 2021; Mishenina et al. 2021), and elemental abundance versus condensation temperature (T_c) relations in planet-hosting stars (e.g., da Silva et al. 2015; Bedell et al. 2018; Liu et al. 2020; Cowley et al. 2021; Mishenina et al. 2021). The large sample of homogeneously investigated comparison stars in our study allows us to take into account spatial and temporal factors as well as other specificities of the Galactic and stellar evolution.

2. Observations and Method of Analysis

2.1. Observations and Target Selection

Observations were carried out with the 1.65 m telescope at the Moletai Astronomical Observatory of Vilnius University in Lithuania, which is equipped with the high-resolution Vilnius University Echelle Spectrograph (VUES; Jurgenson et al. 2016). This spectrograph has a wavelength coverage from 400 to 900 nm in $R \sim 36{,}000$, ~51,000, and ~68,000 resolution modes. For our work, we used the ~68,000 mode for the M spectral type stars and the ~36,000 mode for other objects. Exposure times varied between 900 and 2400 s and signal-to-noise ratios (S/Ns) varied between 75 and 200 with a median value at 96, depending on stellar magnitudes. The VUES data reduction was accomplished on site using the automated pipeline described by Jurgenson et al. (2016).

Like in Paper I, we selected all bright ($V < 8$ mag) F5 and cooler than $T_{\rm eff} < 6500$ K (corresponding to approximately

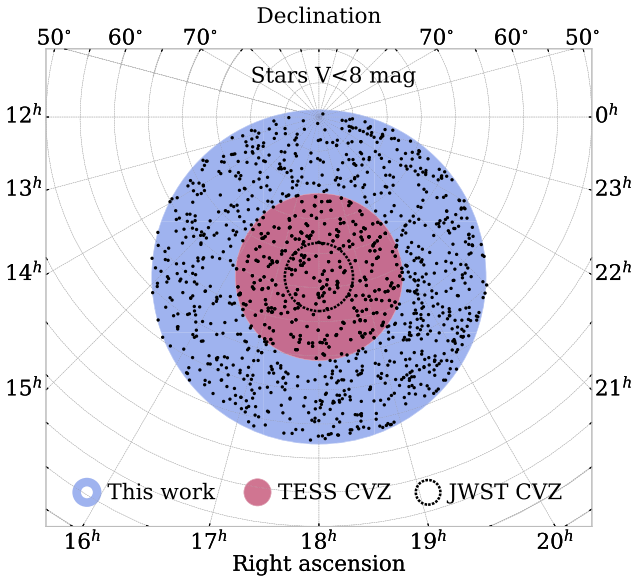

Figure 1. Positions (R.A. and decl. in hours and degrees) of the stars (black dots) observed in this work (blue shadowed area) and in Paper I (pink shadowed area) in the TESS CVZ. The JWST CVZ is indicated as well.

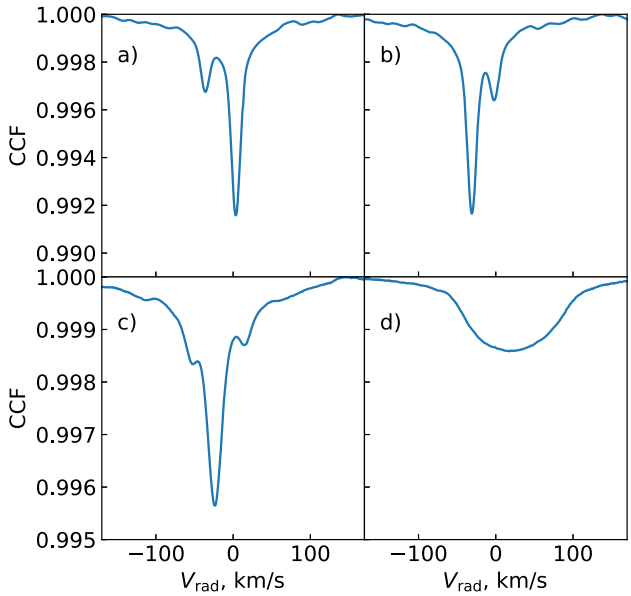

Figure 2. Examples of CCFs produced to calculate the radial velocities and detection of double-line binary stars: (a) the double-line spectroscopic binary HD 152274 observed on 2018 September 19, (b) the same HD 152274 star observed on 2019 June 28, (c) HD 160780 showing three profiles, and (d) the fast-rotating system HD 193341.

$(B-V) > 0.39$ mag) stars in the area surrounding previously observed TESS northern CVZ up to 12° around the northern ecliptic pole. In this way, we found 848 stars in the selected field that met these criteria (see Figure 1), and we have observed all of them during the period of 2019–2021.

2.2. Radial Velocity Determination and Identification of Double-line Binaries and Fast-rotating Stars

For an initial spectral analysis, we used the standard cross-correlation function (CCF) method to obtain spectroscopic radial velocity values. The CCF revealed 27 double-line and one triple-line stellar systems. All 28 stars with double or multiple-line features are recognized as binary systems from proper motion anomaly in Gaia and Hipparcos data (Kervella et al. 2019). Of the 28, 13 are already labeled as spectroscopic binaries, e.g., in the Geneva–Copenhagen survey (Nordström et al. 2004) or in the SIMBAD database (Wenger et al. 2000). The remaining 15 stars are newly detected spectroscopic binaries. Figure 2 shows the CCF examples of our study. The CCF also revealed 33 fast-rotating stars ($V_{\rm rot} \geqslant 20$ km s^{-1}) with strongly broadened and diminished lines that prevented us from analyzing them. From the subsequent analysis, we also excluded the 47 coolest (M-type) stars with severe line-blending. We postponed a further investigation of these stars. This investigation requires different methods of analysis and additional photometric and spectral observations.

Thus, of the observed 848 stars, we fully characterized a sample of 740 stars.

2.3. Stellar Atmospheric Parameters and Chemical Composition

In order to determine the main stellar atmospheric parameters (effective temperature, $T_{\rm eff}$; surface gravity, $\log g$; microturbulence velocity, $v_{\rm t}$; and metallicity [Fe/H]), we adopted the classical method of the equivalent widths of atomic neutral and ionized iron lines. We used a combination of the DAOSPEC (Stetson & Pancino 2008) and MOOG (Sneden 1973) codes in the same way as the Vilnius node used in the Gaia-ESO Survey (see Smiljanic et al. 2014 and Mikolaitis et al. 2018).

Detailed abundances of 24 chemical species were determined by applying a spectral synthesis method with the TURBOSPECTRUM code (Alvarez & Plez 1998). The spectral analysis was done using a grid of MARCS stellar atmosphere models (Gustafsson et al. 2008) and the solar abundances by Grevesse et al. (2007). Atomic lines were selected from the Gaia-ESO line-list by Heiter et al. (2015). We have also used the molecular line lists for C_2 (Brooke et al. 2013; Ram et al. 2014), CN (Sneden et al. 2014), CH (Masseron et al. 2014), SiH (Kurucz 1993), FeH (Dulick et al. 2003), CaH (B. Plez 2022, private communication), and OH, MgH, and NH (T. Masseron 2022, private communication). For the carbon abundance determination, we used two regions: the C_2 Swan (1, 0) band head at 5135 Å and the C_2 Swan (0, 1) band head at 5635 Å. For the nitrogen abundance determination, we used $^{12}C^{14}N$ molecular lines in the regions 6470–6485 and 7980–8005 Å. The oxygen abundance was determined from the forbidden [O I] line at 6300 Å. These elements require a more detailed analysis, as they are bound by the molecular equilibrium. First, we performed several iterations until the determinations of carbon and oxygen abundances converged. After this, we used both carbon and oxygen values to determine the abundance of nitrogen.

In Figure 3 we show examples of the observed and modeled C_2, CN, and [O I] line fits. For more details of the chemical composition analysis, we refer to Paper I and other recent studies (Mikolaitis et al. 2019; Stonkutė et al. 2020).

2.4. Stellar Ages

In order to calculate stellar ages, we used the code UniDAM (the unified tool to estimate distances, ages, and masses) by Mints & Hekker (2017, 2018). The code uses a Bayesian approach and the PARSEC isochrones (Bressan et al. 2012). As an input, we used the stellar atmospheric parameters

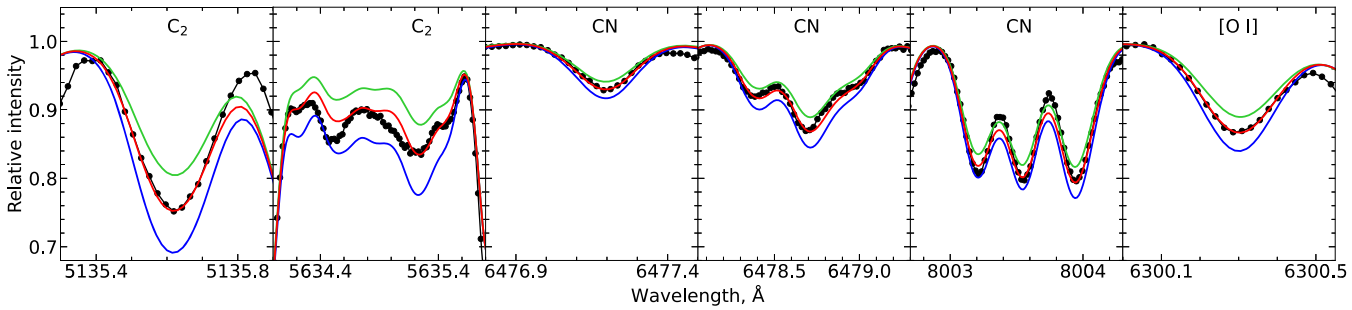

Figure 3. Examples of synthetic spectrum fits to the C_2 band heads at 5135 and 5635 Å, to the CN bands at 6478 and 8003 Å, and to the forbidden [O I] line at 6300 Å. The observed spectra are shown as solid black lines with dots. The solid red lines represent the best fits, while the solid blue and green lines represent a change in abundance by ±0.1 dex of the corresponding elements.

determined in this work together with the *J*, *H*, and *K* magnitudes from the Two Micron All-Sky Survey (2MASS; Skrutskie et al. 2006) and the W1 and W2 magnitudes from AllWISE (Cutri et al. 2014).

We cross-matched our sample of 740 stars with the 2MASS and AllWISE catalogs and obtained 715 objects with entries in both databases. After calculating the ages, we discarded 137 stars for which the reported flags meant either an unreliable photometry, that the result was off the model grid, or just an unreliable determination (see Section 6.1 in Mints & Hekker 2017 for more interpretations). Finally, we were left with 578 stars for which we report the derived ages in this work. However, one should take into account that uniDAM assumes a scaled solar abundance pattern, and this can introduce a bias in the age estimates when this assumption is wrong.

2.5. Kinematic Properties

The main kinematic parameters ($R_{\rm mean}$, $z_{\rm max}$, *e*, *U, V,* and W) for the stars were calculated using the Python-based package for galactic-dynamics calculations *galpy*[3] by Bovy (2015). We used two main sources for the input data: the distances were taken from Bailer-Jones et al. (2021), whereas proper motions, coordinates, and radial velocities were taken from the Gaia data release 3 (EDR3) catalog (Gaia Collaboration et al. 2016, 2021; Lindegren et al. 2021; Seabroke et al. 2021). The radial velocities of 686 stars were taken from the Gaia EDR3, and those of the remaining 54 were gathered either from the SIMBAD database or from our own determinations. Several stars did not have proper motion values in the EDR3. In these cases, we used values from the online SIMBAD database.

The *galpy* was set to integrate orbits for 5 Gyr. Observational errors were estimated using 1000 Monte Carlo calculations according to the errors in the input parameters. The position and movements of the Sun are those from Bovy et al. (2012; $R_{\rm gc\odot} = 8$ kpc and $V_\odot = 220$ km s^{-1}), the distance from the Galactic plane is $z_\odot = 0.02$ kpc (Joshi 2007), and the LSR is from Schönrich et al. (2010; *U, V, W* = 11.1, 12.24, 7.25 km s^{-1}).

2.6. Errors on Atmospheric Parameters and Abundances

The errors on the atmospheric parameters and abundances were estimated for every star. The procedure is described in Paper I and in Mikolaitis et al. (2019). Here we briefly recall the main information.

[3] http://github.com/jobovy/galpy

Tests for estimating the impact of the S/N on the error budget in our atmospheric parameter determination and chemical abundance measurements have been made in Paper I for giants and in Mikolaitis et al. (2019) for dwarf stars. We used 300 generated spectra of a star for S/N values of 25, 50, and 75 to determine the atmospheric parameter and measure abundances in order to estimate their sensitivity to the quality of the spectrum.

Evaluation of the line-to-line scatter is a way to estimate random errors if the number of lines is large enough. A median of the standard deviation for a given element, $\sigma^*_{\rm scat}$, is presented in the sixth column of Table 1.

The uncertainties of the main atmospheric parameters were propagated into the errors of chemical abundances. The median errors of this type over the stellar sample are provided in Table 1.

The final error for every element for every star that is given in the machine-readable Table A1 is a quadratic sum of the effects due to the uncertainty in four atmospheric parameters and the abundance scatter given by the lines.

In this paper, we use a classical local thermodynamic equilibrium (LTE) approach for all lines of the studied elements. In the metallicity range of our sample stars, non-LTE effects should be small (see Section 3.6 of Mikolaitis et al. 2019 and references therein). As we focus on [C/O] and [Mg/Si] later in the paper, it is worthwhile mentioning that the C_2 bands that were used to determine the carbon abundance are not sensitive to non-LTE deviations (Clegg et al. 1981; Gustafsson et al. 1999). The 6300.3 Å oxygen forbidden line is known to be unaffected by non-LTE and shows little sensitivity to 3D effects (Asplund 2004; Pereira et al. 2009). This line forms nearly in LTE and is only weakly sensitive to convection, its formation is similar in 3D radiation hydrodynamic and 3D magnetoradiation-hydrodynamical solar models (Bergemann et al. 2021). Therefore, possible non-LTE effects on [C/O] should be very small. It was shown by Adibekyan et al. (2017) that the non-LTE effect on the [Mg/H] ratio is expected to be from −0.01 to 0.03 dex, and for [Si/H] from −0.004 to 0.012 dex. This leads to a possible non-LTE correction for [Mg/Si] of 0.0 to 0.03 dex in a metallicity regime similar to that of our sample. For manganese and copper, we have accounted for hyperfine splitting as described in Mikolaitis et al. (2019).

Since the abundances of C, N, and O are bound together by the molecular equilibrium in the stellar atmospheres, in Paper I we investigated how an error in one of them typically influences the abundance determination of another. We determined that Δ[O/H] = 0.10 causes Δ[C/H] = 0.02 and

Table 1
Median Effects on the Derived Abundances Resulting from the Atmospheric Parameter Uncertainties for the Sample Stars

El	$\Delta T_{\rm eff}$ (K)	$\Delta \log g$	Δ[Fe/H]	$\Delta v_{\rm t}$ (km s^{-1})	$\sigma_{\rm scat}$[a]	$N_{\rm max}$[b]	$\sigma_{\rm total}\left[\frac{\rm El}{\rm H}\right]$[c]	$\sigma_{\rm all}\left[\frac{\rm El}{\rm H}\right]$[d]
C(C_2)	0.00	0.03	0.01	0.01	0.02	2	0.03	0.04
N(CN)	0.06	0.05	0.01	0.01	0.05	7	0.08	0.09
O([O I])	0.01	0.08	0.07	0.00	0.06	1	0.11	0.12
Na I	0.01	0.03	0.03	0.02	0.06	4	0.05	0.08
Mg I	0.02	0.07	0.03	0.03	0.07	5	0.08	0.11
Al I	0.02	0.03	0.03	0.03	0.08	5	0.06	0.10
Si I	0.01	0.02	0.02	0.02	0.05	14	0.04	0.06
Si II	0.02	0.06	0.02	0.02	0.08	7	0.07	0.11
Ca I	0.03	0.07	0.02	0.02	0.07	28	0.08	0.11
Ca II	0.03	0.06	0.02	0.04	0.06	3	0.08	0.10
Sc I	0.05	0.03	0.03	0.03	0.09	7	0.07	0.12
Sc II	0.02	0.07	0.02	0.04	0.05	7	0.09	0.10
Ti I	0.04	0.04	0.02	0.02	0.06	75	0.06	0.09
Ti II	0.01	0.07	0.04	0.04	0.05	19	0.09	0.10
V I	0.03	0.01	0.02	0.04	0.06	8	0.05	0.08
Cr I	0.02	0.03	0.02	0.03	0.06	7	0.05	0.08
Cr II	0.02	0.07	0.02	0.04	0.05	2	0.09	0.10
Mn I	0.03	0.03	0.02	0.04	0.06	14	0.06	0.09
Fe I	0.01	0.03	0.02	0.03	0.04	137	0.05	0.06
Fe II	0.01	0.08	0.03	0.04	0.07	11	0.09	0.12
Co I	0.01	0.01	0.01	0.02	0.07	7	0.03	0.07
Ni I	0.01	0.02	0.01	0.04	0.05	30	0.05	0.07
Cu I	0.03	0.02	0.02	0.02	0.07	6	0.05	0.08
Zn I	0.02	0.02	0.03	0.03	0.10	3	0.05	0.12

Notes.
[a] $\sigma_{\rm scat}$ stands for the median line-to-line scatter.
[b] $N_{\rm max}$ presents the number of lines investigated.
[c] $\sigma_{\rm total([El/H])}$ stands for the median of the quadratic sum of all four effects on [El/H].
[d] $\sigma_{\rm all([El/H])}$ is a median of the combined effect of $\sigma_{\rm total([El/H])}$ and the line-to-line scatter $\sigma_{\rm scat}$.

Δ[N/H] = 0.04, and Δ[C/H] = 0.10 causes Δ[N/H] = −0.11 and Δ[O/H] = 0.02, while Δ[N/H] = 0.10 has no effect on either the carbon or the oxygen abundances.

3. Stellar Parameters

The determined stellar parameters are presented in Table A1 (which is available in its entirety in machine-readable form) and are discussed in the following sections.

3.1. Stellar Ages, Kinematic Properties, and Dependence on Galactic Subcomponents

The ages of our sample stars range from about 0.2 to 12 Gyr; the majority are close to solar, about 5 Gyr. The age values and uncertainties are presented in Table A1.

The U, V, and W velocities, distances, $R_{\rm mean}$, $z_{\rm max}$, and orbital eccentricities, e, with the corresponding errors are presented in Table A1.

It is widely accepted that Galactic subcomponents such as thin and thick disks differ in a number of parameters. There are two widely used methods to separate them: kinematical (e.g., Bensby et al. 2003, 2005, 2014) and chemical (e.g., Adibekyan et al. 2012b; Recio-Blanco et al. 2014).

The method introduced by Bensby et al. (2003, 2014) employs the thick-disk (TD) to thin-disk (D) probability ratios. Stars with TD/D > 2 are potential thick-disk stars, stars with TD/D < 0.5 potentially belong to the thin disk, and stars with 0.5 < TD/D < 2.0 are called "in-between stars". We provide this TD/D value in Table A1 as well.

The chemical separation method can employ [Mg I/Fe I] (Adibekyan et al. 2012b; Mikolaitis et al. 2014), [Ti I/Fe I] (Bensby et al. 2014), or [α/Fe I] (Recio-Blanco et al. 2014) abundance ratios. Recently, Lagarde et al. (2021) have proposed the age-chemo-kinematics approach, which we applied in this work as well. We used [Mg I/Fe I] and [α/Fe I] versus [Fe I/H] to separate the low-α from high-α stars that potentially belong to the thin or thick disks, respectively. The values of [α/Fe I], which are averages of Mg I, ⟨Si I, Si II⟩, ⟨Ca I, Ca II⟩, ⟨Ti I, Ti II⟩, and the standard errors of the mean are presented in columns 77 and 78 of Table A1.

Based on chemical signatures, we thus separated our sample of stars into 601 thin-disk, 138 thick-disk, and one high-α halo star.

Recently, studies have emerged that showed that the thick-disk stars can be even further divided into separate populations of metal-rich and metal-poor stars. The exact nature of the high-α metal-rich (hαmr) stars is still debated, but a few explanations have been proposed. One of them (Sharma et al. 2021; Zhang et al. 2021) is that these stars were born somewhere at the edge of the Bulge, at around 3–5 kpc from the Galactic center, and later migrated outward. Zhang et al. (2021) discussed that the radial migration induced by the coupling between the bar and the spiral arms could bring its stars from the birth sites of 3–5 kpc to their current locations.

When analyzing the APOKASC sample of stars, Lagarde et al. (2021) found two density peaks in the [α/Fe] versus [Fe/H] plane for thick-disk stars. They determined that the kinematics of the hαmr thick-disk population seems to follow that of the thin-disk population more closely than that of the

hαmp thick-disk population and came to a similar conclusion as Sharma et al. (2021) and Zhang et al. (2021) that these properties might suggest a different origin and history for these stars by migration from the inner disk or as a transition region between the old thick disk and the young thin disk.

The equations for separating the thick-disk components were derived in the work by Lagarde et al. (2021). These equations somewhat depend on the spectroscopic survey, but they worked well in our case, and the thick and thin disks separate quite nicely. We use the chemical separation in our further discussion. As the analysis of thick-disk subpopulations is not the goal of this paper, we treated the thick disk as a single population. However, in the last column of Table A1, we identify the stars that according to our analysis could be attributed to the hαmr component as well.

3.2. Atmospheric Parameters and Elemental Abundances

Our sample of 740 slowly rotating stars has temperatures $T_{\rm eff}$ between 3977 and 6414 K with a mean of 4703 K. The metallicities [Fe/H] are from −2.25 to 0.15 dex with a mean at −0.34 dex, and the surface gravity $\log g$ is from 0.51 to 3.5 with a mean of 2.4 for giants and from 3.6 to 4.48 with a mean of 4.0 for dwarfs.

Atmospheric parameters are listed in the Table A1 together with elemental abundances (C(C_2), N(CN), [O I], Na I, Mg I, Al I, Si I, Si II, Ca I, Ca II, Sc I, Sc II, Ti I, Ti II, V I, Cr I, Cr II, Mn I, Fe I, Fe II, Co I, Ni I, Cu I, and Zn I) relative to the Sun and their uncertainties for the 740 stars investigated in the present study. The abundances are presented in [Element/H] form.

Our derived main atmospheric parameters and chemical abundances of many elements complement other large spectroscopic catalogs of, e.g., Delgado Mena et al. (2021) and Bensby et al. (2014), among others, because we do not have stars in common with these high-resolution spectroscopic catalogs. We have only one star in common in our study and that of Bensby et al. (2014), and the parameters of this star agree well.

In the compilation of the PASTEL catalog (Soubiran et al. 2016), we found a few studies that have derived stellar parameters for some stars of our sample. PASTEL is a bibliographical catalog that compiles determinations of stellar atmospheric parameters ($T_{\rm eff}$, $\log g$, and [Fe/H]) and provides determinations obtained from detailed analyses of high-resolution spectra with high S/N. It provides atmospheric parameters derived from various methods. We have 107 stars in common that were observed before with derived main atmospheric parameters that are collected in the PASTEL catalog. The consistency of the effective temperature and surface gravity in our sample and PASTEL (catalog version of 2020 January 30 as in VizieR) is quite good: $\langle \Delta T_{\rm eff} \rangle = 36 \pm 92$ K and $\langle \Delta \log g \rangle = 0.15 \pm 0.41$. The scatter of $\Delta \log g$ is caused by the variety of surface gravity determination methods (e.g., different line lists) that were used for the values presented in the PASTEL compilation.

We found 55 stars in common with the 16th data release (DR16) of the near-infrared, large-scale, stellar spectroscopic survey APOGEE (Jönsson et al. 2020). For the comparison of the two studies, we used the calibrated parameters and abundances determined with the APOGEE Stellar Parameters and Chemical Abundance Pipeline (ASCAP, version l33, release 12; García Pérez et al. 2016). The biases for the main

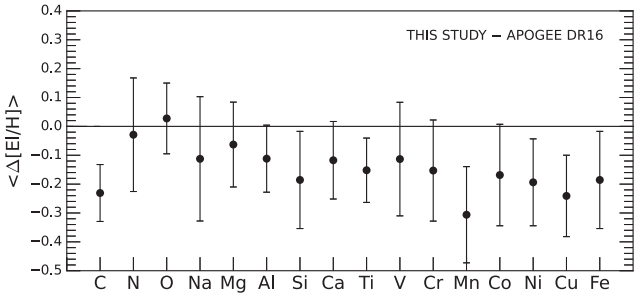

Figure 4. Comparison of abundances for the 55 stars in common with APOGEE DR16. The average differences and standard deviations are calculated as our results minus the comparison.

stellar atmospheric parameters from our sample are $\langle \Delta T_{\rm eff} \rangle = -23 \pm 93$ K and $\langle \Delta \log g \rangle = 0.07 \pm 0.29$ dex. Having in mind that a complex approach of calibration was adopted to determine the surface gravity in the APOGEE survey (see Jönsson et al. 2020 Section 5.2.2 for more details), the agreement between our results is rather good.

In Figure 4 we show our comparison of [Element/H] abundances for the 55 stars in common with APOGEE DR16. The average differences for all stars in common and the standard deviations are calculated as our results minus the comparison. The sample of common stars is not very large; however, as one can see, the majority of elements have a systematic shift of about −0.15 dex. We refer the reader to Jönsson et al. (2020) and their Table 12, where APOGEE DR16 results were compared with independent high-resolution optical spectroscopic works. It was found that DR16 also has an average shift of about −0.05 dex compared to the other optical studies.

Regarding the C, N, and O elements, the APOGEE survey DR16 uses the infrared lines of CO, CN, and OH molecules, respectively, and the agreement for the nitrogen and oxygen abundances is quite good. The abundances of carbon, on the other hand, differ by about 0.2 dex. The larger carbon abundances determined in the APOGEE survey could be caused by the weakness of the investigated CO bands and by difficulties in the placement of the continuum.

4. Star–Planet Connections

A list of 25 planet-hosting stars with their C/O, Mg/Si abundance ratios, [Fe I/H], and information about their planets is presented in Table 2. The planetary mass ($M_p \sin i$) and orbital period (in days) were taken from the NASA Exoplanet Archive on 2021 December 15. The references are provided in Table 2. Stars HD 158259, HD 7924, and HD 21652 host five, three, and two low-mass planets, respectively. Star HD 164922 has three low-mass and one high-mass planets. Three more stars have two confirmed high-mass planetary systems. According to Kokaia et al. (2020), stars HD 154345 and HD 150709 may be candidate systems with high resilient habitability and have good prospects for the detection of planets in their habitable zones. According to Agnew et al. (2018), ψ 1 Dra also has as high 0%–25% probability of resilient habitability. In our sample, the two planet-hosting stars HD 155358 and HD 145675 belong to the thick disk of the Galaxy (one belongs to the metal-poor and one to the metal-rich parts), and all the remaining stars are the thin-disk stars.

Table 2
Stars of Our Sample with Confirmed Exoplanets

TYC ID	Planet	Planet Mass ($M_{\rm Earth}$)	Planet Mass ($M_{\rm Jupiter}$)	Orbital Period (days)	References	C/O	Mg/Si	[Fe I/H]
2099-2717-1	HD 164922 b	116^{+10}_{-12}	$0.365^{+0.031}_{-0.038}$	1207^{+4}_{-5}	1	0.59 (a)	1.44 (b)	0.17 (b)
	HD 164922c	13^{+3}_{-2}	$0.041^{+0.009}_{-0.006}$	$75.74^{+0.06}_{-0.05}$	1			
	HD 164922 d	4 ± 1	0.01 ± 0.00	12.458 ± 0.003	1			
	HD 164922 e	10.5 ± 1.0	0.0331 ± 0.0031	41.763 ± 0.012	2			
2103-1620-1	HD 164595 b	16.14 ± 2.72	0.05078 ± 0.00856	40 ± 0.24	3	⋯	1.05 (b)	−0.13 (b)
2595-1464-1	HD 155358 b	315 ± 25	0.99 ± 0.080	194.3 ± 0.30000	4	0.26 (a)	1.55 (b)	−0.66 (b)
	HD 155358c	261 ± 22	0.82 ± 0.07	391.9 ± 1.0	5			
2648-2151-1	HD 178911 B b	2552 ± 798	8.03 ± 2.510	71.484 ± 0.02000	4	⋯	1.08 (b)	0.20 (b)
3067-576-1	14 Her b	1481 ± 48	4.66 ± 0.15	1773.40002 ± 2.50000	4	⋯	1.60 (b)	0.33 (b)
	HD 145675c	1843^{+445}_{-318}	$5.8^{+1.4}_{-1.0}$	25000^{+24000}_{-9200}	2			
3501-1373-1	HD 154345 b	261 ± 22	0.82 ± 0.07	3341.55884 ± 93.00000	4	⋯	0.95 (b)	−0.13 (b)
3525-186-1	HD 168009 b	$9.53^{+1.21}_{-1.18}$	$0.03^{+0.0038}_{-0.0037}$	$15.1479^{+0.0035}_{-0.0037}$	2	0.62 (b)	1.23 (b)	−0.01 (b)
3565-1525-1	16 Cyg B b	566 ± 25	1.78 ± 0.08	798.5 ± 1.00000	4	0.55	1.15	−0.05
3869-494-1	HD 139357 b	3101.89 ± 683.306	9.76 ± 2.150	1125.7 ± 9.000	6	0.3	1.09	0.23
3875-1620-1	iot Dra b	2803.1 ± 228.8	8.82 ± 0.72	511.098 ± 0.089	7	0.32	0.99	−0.05
3888-1886-1	HD 158259 b	$2.22^{+0.39}_{-0.45}$	$0.00698^{+0.00123}_{-0.00142}$	$2.178^{+0.00009}_{-0.00010}$	8	0.61 (b)	1.17 (b)	−0.07 (b)
	HD 158259c	$5.6^{+0.60}_{-0.59}$	$0.0176^{+0.0019}_{-0.0019}$	$3.432^{+0.00030}_{-0.00016}$	8			
	HD 158259 d	$5.41^{+0.74}_{-0.71}$	$0.017^{+0.0023}_{-0.0022}$	$5.1980814^{+0.0008186}_{-0.0008814}$	8			
	HD 158259 e	$6.08^{+0.94}_{-1.03}$	$0.0191^{+0.0030}_{-0.0032}$	$7.951^{+0.0022}_{-0.0021}$	8			
	HD 158259 f	$6.14^{+1.31}_{-1.37}$	$0.0193^{+0.0041}_{-0.0043}$	12.028 ± 0.009	8			
3903-2143-1	HD 167042 b	$540.29^{+28.60}_{-38.14}$	$1.7^{+0.9}_{-0.12}$	$420.77^{+3.48}_{-3.11}$	9	0.32	1.05	−0.01
3910-257-1	HD 163607 b	249.1 ± 3.1	0.7836 ± 0.0098	75.2203 ± 0.0094	10	0.50 (c)	1.17 (c)	0.17 (c)
	HD 163607c	699.5 ± 11.8	2.201 ± 0.037	1272 ± 4.4	10			
4222-2311-1	42 Dra b	1233.13 ± 270.14	3.88 ± 0.85	479.1 ± 6.2	6	0.28 (c)	1.23 (c)	−0.47 (c)
4412-1654-1	HD 143105 b	385 ± 19	1.21 ± 0.06	2.1974 ± 0.0003	11	0.51	1.15	−0.07
4414-2315-1	11 UMi b	4685 ± 795	14.74 ± 2.50	516.21997 ± 3.20000	4	0.24	0.95	−0.34
4416-1799-1	bet UMi b	1938.7 ± 317.8	6.1 ± 1.0	522.3 ± 2.7	12	0.19	1.03	−0.50
4417-267-1	8 UMi b	416 ± 51	1.31 ± 0.16	93.4 ± 4.50000	4	0.14	1.32	−0.16
4436-1424-1	psi 1 Dra B b	486 ± 32	1.53 ± 0.10	3117 ± 42	13	0.55 (a)	1.29 (b)	−0.08 (b)
4494-1346-1	HD 7924 b	6.4 ± 0.00	0.02 ± 0.00	5.39792 ± 0.00025	4	0.44 (a)	1.23 (b)	−0.30 (b)
	HD 7924c	$7.86^{+0.73}_{-0.71}$	$0.0247^{+0.0023}_{-0.0022}$	$15.299^{+0.0032}_{-0.0033}$	14			
	HD 7924 d	$6.44^{+0.79}_{-0.78}$	$0.0203^{+0.0025}_{-0.0025}$	$24.451^{+0.015}_{-0.017}$	14			
4532-2096-1	HD 33564 b	2892.1	9.1	388 ± 3	15	⋯	1.11 (b)	−0.16 (b)
4561-2319-1	HD 120084 b	1430.2	4.5	2082^{+24}_{-35}	16	0.30	1.28	−0.07
4575-1336-1	HD 150706 b	$861.28^{+362.31}_{-209.76}$	$2.71^{+1.14}_{-0.66}$	5894^{+5584}_{-1498}	17	0.45 (a)	1.12 (b)	−0.15 (b)
4576-1486-1	HD 158996 b	4450 ± 731	14 ± 2.3	820.2 ± 14.0	18	0.19	0.97	−0.47
4650-917-1	HD 216520 b	10.26 ± 0.99	0.03228 ± 0.00311	35.45 ± 0.011	19	0.40 (a)	1.10 (b)	−0.35 (b)
	HD 216520c	9.44 ± 1.630	0.0297 ± 0.00513	154.43 ± 0.44	19			

Note. Some host C, O, Mg, and Si elemental abundances are taken from our previous works: (a) Stonkutė et al. (2020), (b) Mikolaitis et al. (2019), and (c) Tautvaišienė et al. (2020).

References. Planet mass and period references: 1—Benatti et al. (2020), 2—Rosenthal et al. (2021), 3—Courcol et al. (2015), 4—Stassun et al. (2017), 5—Robertson et al. (2012), 6—Döllinger et al. (2009), 7—Butler et al. (2006), 8—Hara et al. (2020), 9—Bowler et al. (2010), 10—Luhn et al. (2019), 11—Hébrard et al. (2016), 12—Lee et al. (2014), 13—Endl et al. (2016), 14—Fulton et al. (2015), 15—Galland et al. (2005), 16—Sato et al. (2013), 17—Boisse et al. (2012), 18—Bang et al. (2018), 19—Burt et al. (2021).

4.1. Stellar Chemical Composition and Planet Mass Relation

Figure 5 displays the distributions of parameters and elemental abundances in planet-hosting stars and planets as a function of planet masses. We marked planets orbiting dwarfs and giants as well as thin- and thick-disk stars with different symbols. Along with our sample, we also display the results from the recent study by Mishenina et al. (2021). We updated the parameters of planets in their study according to the NASA Exoplanet Archive data of 2021 December 15 and computed $R_{\rm mean}$ and $z_{\rm max}$ for their host stars. All the investigated stars in that study are thin-disk dwarfs.

According to the mass, the exoplanets fall into two widely separated mass ranges (Figure 5(a)). One group of planets has masses from 2.22 to 16.14 $M_{\rm Earth}$ (we call them low-mass planets), and another group is from 116 to 3102 $M_{\rm Earth}$ (high-mass planets).

The values of $R_{\rm mean}$ in our sample of planet-hosting stars range from 6.22 to 9 kpc, except for one star that is located at 11.66 kpc. The $z_{\rm max}$ values are up to 0.57 kpc, except for one star with four planets, which is at 0.96 kpc.

When we compare the metallicity (Figure 5(d)), it is on average higher by about 0.2 dex in dwarfs with confirmed high-mass planets than in dwarfs with low-mass planets. This is in

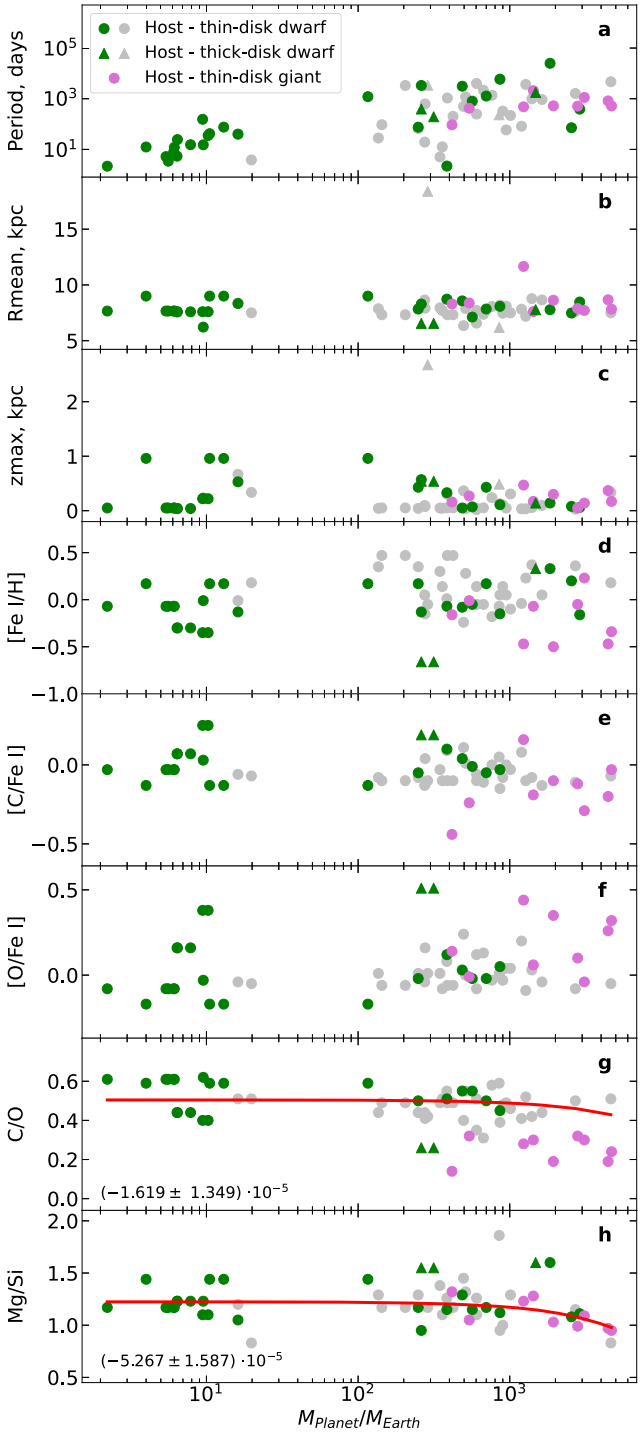

Figure 5. Distributions of parameters and elemental abundances in planet-hosting stars and planets as a function of planet masses. The green symbols indicate the planet-hosting dwarfs, the pink symbols are for giants, and the gray symbols are for dwarfs investigated by Mishenina et al. (2021). The circles indicate thin-disk stars, and the triangles are for thick-disk stars. See the text for more information.

agreement with findings by Adibekyan et al. (2012b). However, there are giant stars of lower metallicity with high-mass planets, but we do not have giants with confirmed low-mass planets in our sample for a comparison. A comprehensive review of the metallicity of planet-hosting stars can be found in Adibekyan (2019).

We also searched for signatures of different carbon and oxygen abundances in low- and high-mass planet-hosting stars. We found no significant correlation between carbon or oxygen abundances and planetary masses. The same conclusion concerning carbon was reached by Suárez-Andrés et al. (2017).

Of course in giants, the carbon abundances are lower by about 0.2 dex than in dwarfs due to material mixing effects in evolved stars (see Tautvaišienė et al. 2010), and the oxygen abundances are larger due to the lower stellar metallicity and the corresponding Galactic chemical evolution results, and the C/O ratios, consequently, are lower by about 0.25.

We computed the linear fits for the C/O and Mg/Si versus planetary mass similar to Mishenina et al. (2021), and we used their data to compliment ours (Figures 5(g) and (h)). Our sample has more dwarfs with low-mass planets, while with complementary giants, we added more stars with high-mass planets to the sample, which can be used to compute the Mg/Si slope. We find a weak negative C/O slope with a Pearson correlation coefficient (PCC) equal to −0.17 and a slightly more negative Mg/Si slope with PCC = −0.37 toward the stars with high-mass planets. The Mg/Si versus planetary mass slope is exactly the same as was found by Mishenina et al. (2021). Adibekyan et al. (2015) also suggested that low-mass planets are more prevalent around stars with a high Mg/Si ratio. Suárez-Andrés et al. (2018) also found a slightly negative slope for Mg/Si, but inferred a positive slope for C/O versus planetary mass.

We also looked for similarities or differences between the stars without confirmed planets and the low- and high-mass planet-hosting stars. The abundance ratios of Mg/Si, C/O, and the element abundances [C/Fe], [N/Fe], and [O/Fe] together with α-elements as a function of metallicity are presented in Figure 6. The thin- and thick-disk stars are displayed with different colors, as are the low- and high-mass planet-hosting stars. The [α/Fe] values are computed from the abundances of Mg, Si, Ca, and Ti elements.

Adibekyan et al. (2012a) found that the [El/Fe] ratios for α-elements both for high- and low-mass planet hosts are systematically higher than those of comparison stars at low metallicities ([Fe/H] $\leqslant 0.2$). The stars in our sample confirm this finding (Figure 6(a)).

We found that both planet hosts and non-planet hosts have similar Mg/Si ratios and CNO abundances. We agree with the study by Bedell et al. (2018) that the ratios of carbon-to-oxygen and magnesium-to-silicon in solar-metallicity stars are homogeneous, implying that exoplanets may exhibit a rather small diversity of composition. However, in our sample we can see (the yellow symbols in Figure 6(e)) that slightly higher C/O ratios seem to be present in the dwarfs hosting low-mass planets. Delgado Mena et al. (2021) found tentative evidence that stars with low-mass planets have higher [C/Fe] ratios at lower metallicities than stars without planets at the same metallicity.

The cosmic distribution of Mg/Si for the sample stars is broader than that of C/O. Delgado Mena et al. (2010) found that Mg/Si abundance ratios are higher in stars without confirmed planets. This is not evident in our sample (Figure 6(f)).

The work on elemental abundances in planet-hosting stars has to be continued. Investigations of CNO abundances are especially challenging as there are few spectral features for a

robust abundance determination. An encouraging attempt to use the NH band at 3360 Å was performed by Suárez-Andrés et al. (2016). In this study, the nitrogen distributions for stars with and without planets show that planet hosts are nitrogen rich when compared to single stars. However, it was remarked that given the linear trend between [N/Fe] versus [Fe/H], this fact can be explained as being due to the metal-rich nature of planet hosts. In our study, the nitrogen abundances were determined for 11 high-mass planet-hosting stars, 9 of which are giants and 2 are dwarfs, and no concrete conclusions can be drawn so far.

4.2. Elemental Abundances versus Condensation Temperatures

Differences between elemental abundances in the planet-hosting and comparison stars Δ[El/Fe] as a function of the condensation temperatures of chemical elements is another open topic of discussion. Many studies have reported volatile and refractory element abundance variations in planet-hosting stars and their dependence on the elemental condensation temperatures. This question was addressed for the Sun as one of the first planet-hosting stars because the element abundances can be determined with very high accuracy. Meléndez et al. (2009) found that the Sun shows a characteristic signature with a ∼20% depletion of refractory elements relative to the volatile elements in comparison with the solar twins and that the abundance differences correlate strongly with the condensation temperatures of the elements. However, comparisons of stars in binary systems in which only one of the stars has a detected planet show either an opposite pattern (e.g., Tucci Maia et al. 2014; Saffe et al. 2019) or negligible slopes (e.g., in Liu et al. 2021).

González Hernández et al. (2013) in their study of 29 planet-hosting stars found that solar-type stars with only giant planets with long orbital periods display mostly negative slopes. In the work by Liu et al. (2020), a sample of 16 planet-hosting solar-type stars exhibited a variety of abundance–T_c trends with no clear dependence upon age, metallicity, or T_{eff}. In a sample of 25 planet-hosting dwarf stars, Mishenina et al. (2021) inferred a possible relation between the negative slope and planetary masses. Studies of this topic clearly need more precisely determined data.

Because the investigation of elemental abundance correlation with T_c needs comparison objects, it is difficult to select a proper comparison object of the same age, location in the Galaxy, and atmospheric parameters for single stars that could allow accounting for the stellar and Galactic chemical evolution. Together with our previous studies (Paper I; Mikolaitis et al. 2018, 2019; Stonkutė et al. 2020), the number of our homogeneously analyzed stars has risen to 1266. This gives us the possibility of selecting proper comparison stars to answer the question whether planet-hosting stars show an abundance that is different from that of stars without identified planets. As all the stars were studied homogeneously, we are mostly save from any biases or offsets that could occur when comparing stars. We identified one counterpart for only one planet-hosting star, while for others, up to 13 stars with similar parameters were found. In this case, the mean of all similar stars was taken for comparison. When we searched for similar objects, we aimed for a difference in the T_{eff}, log g, [Fe/H], and v_t values of no more than their determination uncertainties, as well as close R_{mean}, z_{max}, and age values. We took into account the dependence on the Galactic disks as well.

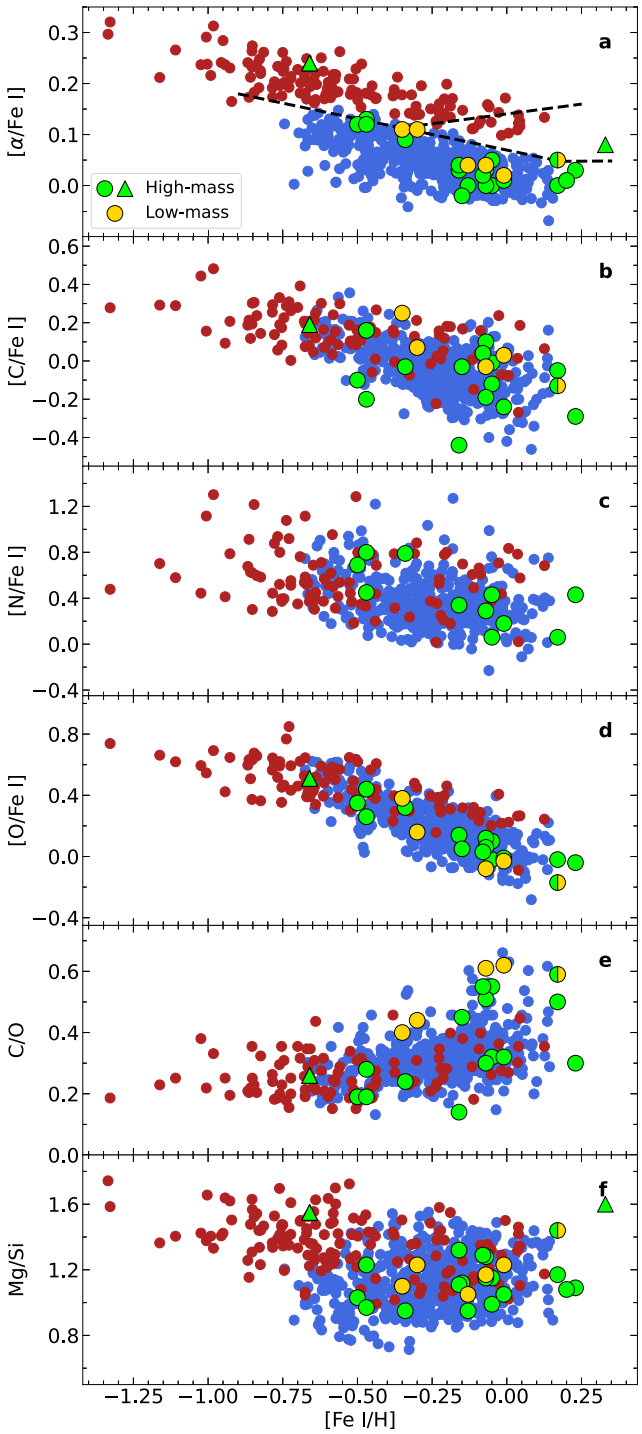

Figure 6. Elemental abundance ratios as a function of metallicity. The blue dots represent the thin-disk stars, and the red dots show the thick-disk. The dashed lines that separate the disks are from Lagarde et al. (2021). The high-mass planet-hosting stars are marked by green symbols (the two belonging to the thick disk are marked by triangles), the stars with low-mass planets are displayed by yellow symbols, and the one with both one high-mass planet and three low-mass planets is shown by the circle filled with both colors.

In Figure 7 we show the differences between elemental abundances Δ[El/Fe] in the planet-hosting and comparison stars as a function of the condensation temperatures of the chemical elements. We mark stars hosting low- and high-mass planets with colored labels, and also mark the one star that

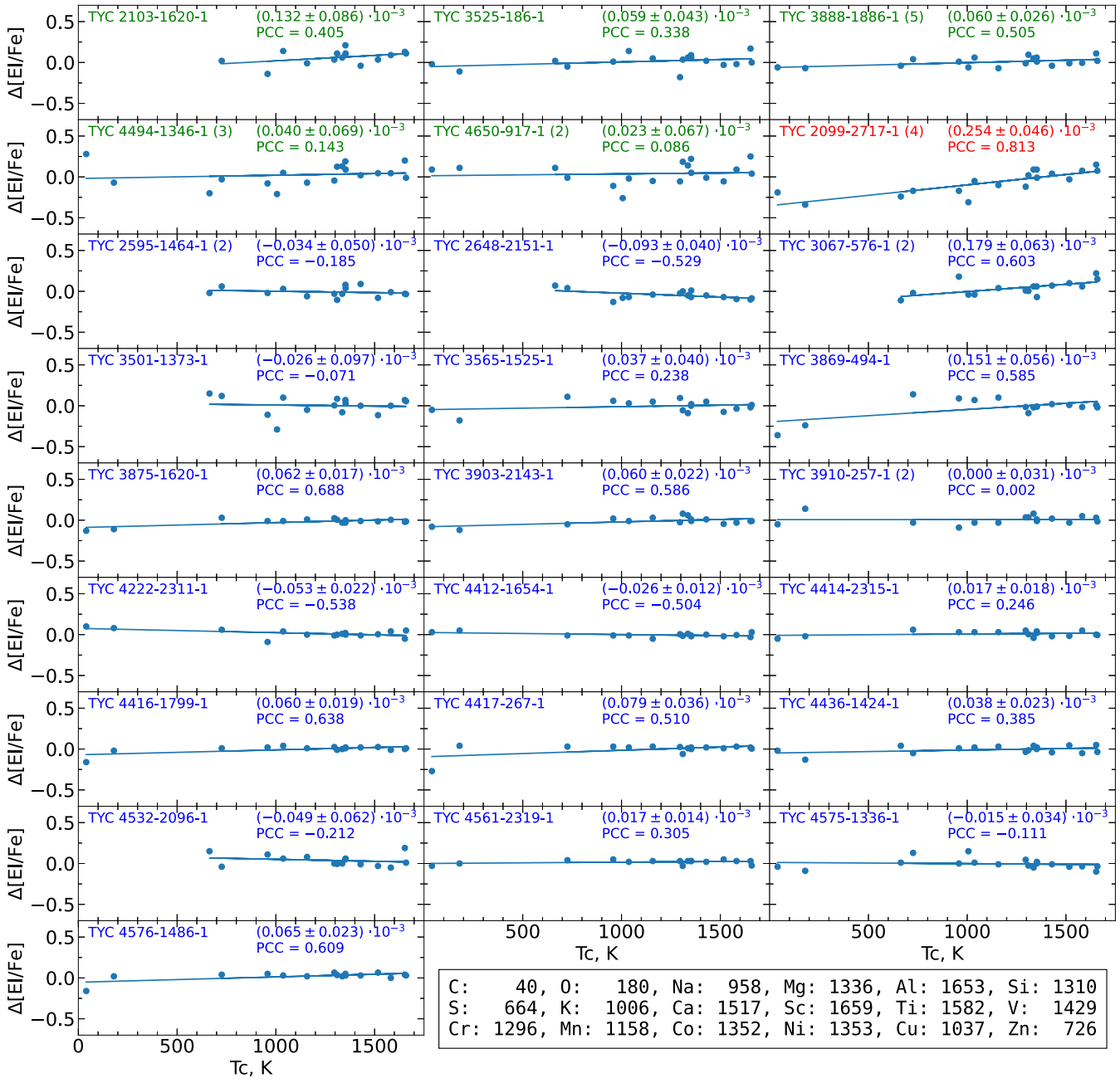

Figure 7. Differences between elemental abundances in the planet-hosting and comparison stars Δ[El/Fe] as a function of the condensation temperatures of chemical elements. The green labels mark stars hosting low-mass planets, the blue labels show stars with high-mass planets, and the red label marks the star with both types of planets. For stars hosting more than one confirmed planet, their number is provided in brackets near the name. The Pearson correlation coefficients and the slopes for the linear regression analysis are displayed in the upper right corners of the plots.

hosts both types of planets (red label). It is easy to notice that the last one shows the largest positive slope. For stars hosting more than one confirmed planet, their number is provided in brackets near the name. The Pearson correlation coefficients and the slopes for the linear regression analysis are displayed in the upper right corners of the plots.

In Figure 8 we show dependences of the Δ[El/Fe]–T_c slopes on the stellar metallicity, age, effective temperature, and planet masses. For stars with several planets, we took their averaged masses. The thin-disk dwarfs and giants as well as the thick-disk dwarfs are marked with different symbols. The size of the symbols represents the number of planets. The red lines display linear fits to the data points, and their Pearson correlation coefficients are presented as labels in the corners of the panels.

All the low-mass planet hosts in our sample show positive slopes in the Δ[El/Fe] versus T_c planes, in particular, the star with the largest number of various planets. Looking at the high-mass planet hosts, we see the diversity of slopes, but our results mean that in more metal-rich, older, and cooler stars, the positive elemental abundance slopes are more common.

We refer to comprehensive theoretical studies concerning possible scenarios of planet formation and star–planet chemical composition relations, which try to incorporate and explain the

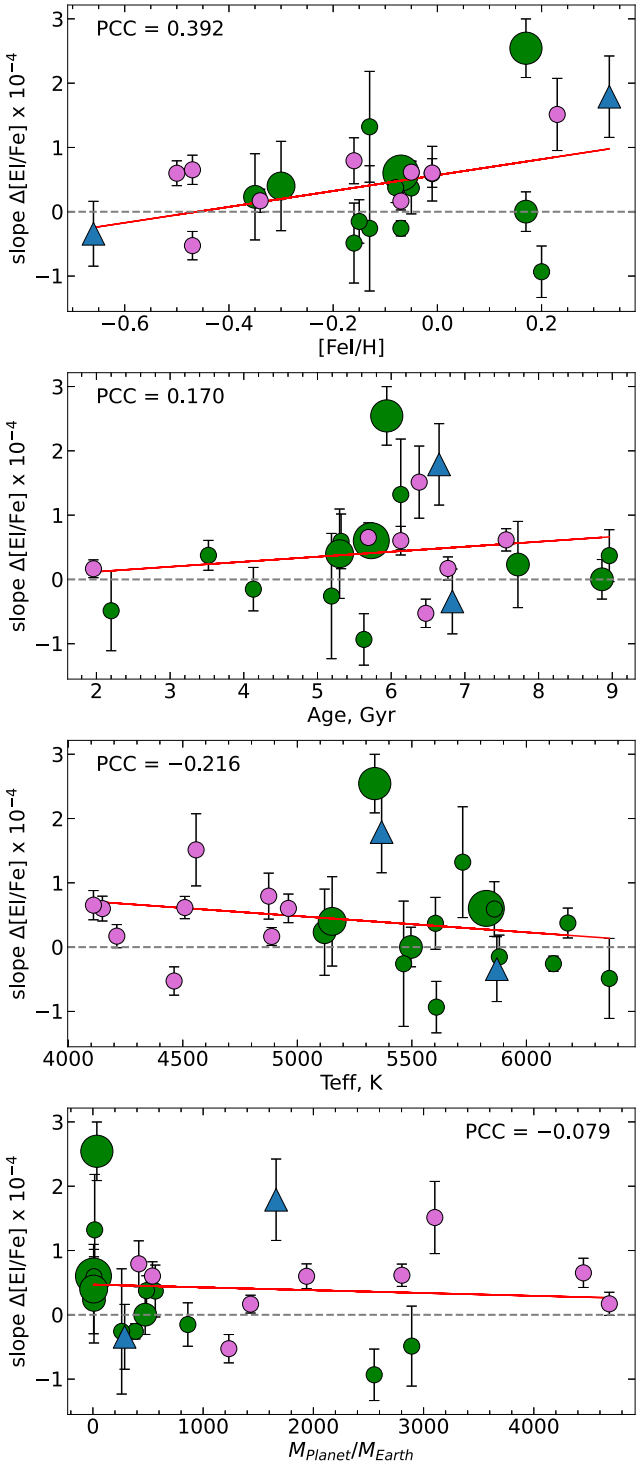

Figure 8. Dependences of Δ[El/Fe]–T_c slopes on the stellar parameters and planet masses. The green circles represent the thin-disk dwarfs, the pink dots show the thin-disk giants, and the thick-disk dwarfs are marked by blue triangles. The size of the symbols depends on the number of confirmed planets in the system. The red lines display linear fits to the data points, and their Pearson correlation coefficients are presented as labels in the corners of the panels.

observational results (e.g., Thiabaud et al. 2015; Bitsch & Battistini 2020; Adibekyan et al. 2021; Cowley et al. 2021; Nibauer et al. 2021; Schneider & Bitsch 2021; Schulze et al. 2021, and references therein).

5. Summary

In this paper, we extended the determination of the main atmospheric parameters, ages, kinematic parameters, and abundances of up to 24 chemical species from high-resolution spectroscopy of bright, ($V < 8$ mag), slowly rotating stars cooler than F5 spectral type in a circle up to about 12° surrounding the northern TESS CVZ.

A detailed characterization was done for a sample of 740 stars of different evolutionary stages, ages, and atmospheric parameters: $T_{\rm eff}$ varied between 3980 and 6400 K, and [Fe/H] varied between −2.25 and 0.15 dex. The stellar ages varied from 0.2 to 12 Gyr. A distinctive log g distribution clearly separated giant and dwarf stars; the parameter of the former varied between 0.5 and 3.5, with a mean at 2.4, while the latter displayed values between 3.6 and 4.5 with a mean at 4.0. Data from the Gaia EDR3 catalog were used to calculate the stellar kinematic parameters. The mean galactocentric distances, $R_{\rm mean}$, span from 4 to 10 kpc, and the distances from the Galactic plane, $z_{\rm max}$, reach 2.4 kpc with $\langle z_{\rm max} \rangle = 0.30 \pm 0.26$ kpc. Stellar velocity components (U, V, and W) were determined as well.

Using a sample of 25 planet-hosting stars, we investigated the stellar chemical composition and planet mass relation, compared elemental abundances with stars without detected planets, and verified elemental abundance versus condensation temperature slopes.

The sample contains stars with five, three, and two low-mass planets. One star has three low-mass planets and one high-mass planet, and three more stars have two confirmed high-mass planetary systems. Three stars may be candidate systems with high resilient habitability and have good prospects for the detection of planets in their habitable zones. Two planet-hosting stars belong to the thick disk of the Galaxy (one belongs to the metal-poor and one to the metal-rich parts), and all the remaining stars are thin-disk stars.

One group of stars hosts planets with masses from 2.22 to 16.14 $M_{\rm Earth}$ (we call them low-mass planets), and another group is from 116 to 3102 $M_{\rm Earth}$ (high-mass planets). The values of $R_{\rm mean}$ in our sample of planet-hosting stars range from 6.22 to 9 kpc, except for one star that is located at 11.66 kpc. The $z_{\rm max}$ values are up to 0.57 kpc, except for one star with four planets that is at 0.96 kpc.

The analysis of planet-hosting stars in our sample drove us to the following conclusions:

1. The dwarf stars hosting high-mass planets are more metal rich than those with low-mass planets.
2. We find a weak negative C/O slope with PCC = −0.17 and a slightly more negative Mg/Si slope with PCC = −0.37 toward the stars with high-mass planets.
3. The element-to-iron ratios for α-elements for high- and low-mass planet hosts are systematically higher than those of comparison stars at lower metallicities.
4. We found that both planet hosts and non-planet hosts have similar Mg/Si ratios and CNO abundances, but slightly higher C/O ratios seem to be present in dwarfs hosting low-mass planets.
5. All the low-mass planet hosts in our sample show positive slopes in the Δ[El/Fe] versus T_c planes, in particular, the star with the largest number of various planets. The high-mass planet hosts have a diversity of slopes.

6. Our results mean that in more metal-rich, older, and cooler stars, positive elemental abundance slopes are more common.

In the rapidly expanding field of exoplanet research, the chemical composition results and information about stellar ages and birth locations determined in this work for stars in the northern hemisphere will provide useful priors in further exoplanet modelings as well as in Galactic evolution studies (see Madhusudhan 2019, 2021; Unterborn & Panero 2019; Hinkel et al. 2020; Clark et al. 2021; Turrini et al. 2021).

We acknowledge the grant from the European Social Fund via the Lithuanian Science Council (LMTLT) grant No. 09.3.3-LMT-K-712-01-0103. The authors would like to thank Dr. Nikku Madhusudhan for the helpful suggestions regarding this project. The anonymous referee is thanked for constructive comments. This research has made use of NASA's Astrophysics Data System Bibliographic Services and SIMBAD database, operated at CDS, Strasbourg, France. This work has made use of data from the European Space Agency (ESA) mission Gaia (https://www.cosmos.esa.int/gaia), processed by the Gaia Data Processing and Analysis Consortium (DPAC, https://www.cosmos.esa.int/web/gaia/dpac/consortium). Funding for the DPAC has been provided by national institutions, in particular the institutions participating in the Gaia Multilateral Agreement. This research has made use of the NASA Exoplanet Archive, which is operated by the California Institute of Technology, under contract with the National Aeronautics and Space Administration under the Exoplanet Exploration Program. We are grateful to the Moletai Astronomical Observatory of Vilnius University for providing observing time for this project.

Facility: NASA Exoplanet Archive.

Software: Astropy (Astropy Collaboration et al. 2018), DAOSPEC (Stetson & Pancino 2008), MOOG (Sneden 1973), galpy (Bovy 2015), TURBOSPECTRUM (Alvarez & Plez 1998), UniDAM (Mints & Hekker 2017).

Appendix
Appendix Information

Table A1 lists the contents of the machine-readable table (atmospheric parameters, kinematic properties, ages, and individual abundances) together with associated errors, and other information for the investigated stars. This table is available in its entirety in machine-readable form.

Table A1
Contents of the Machine-readable Table

Col	Label	Units	Explanations
1	ID	⋯	Tycho catalog identification
2	TESS_ID	⋯	ID in the TESS catalog
3	Teff	K	Effective temperature
4	eTeff	K	Error on effective temperature
5	Logg	dex	Surface gravity
6	e_Logg	dex	Error on surface gravity
7	[Fe/H]	dex	Metallicity
8	e_[Fe/H]	dex	Error on metallicity
9	Vt	km s^{-1}	Microturbulence velocity
10	e_Vt	km s^{-1}	Error on microturbulence velocity
11	Vrad	km s^{-1}	Radial velocity
12	e_Vrad	km s^{-1}	Error on radial velocity
13	Age	log(yr)	Log age of the star
14	e_Age	log(yr)	Error on log age
15	U	km s^{-1}	*U* velocity
16	e_U	km s^{-1}	Error on *U* velocity
17	V	km s^{-1}	*V* velocity
18	e_V	km s^{-1}	Error on *V* velocity
19	W	km s^{-1}	*W* velocity
20	e_W	km s^{-1}	Error on *W* velocity
21	d	kpc	Distance
22	R_{mean}	kpc	Mean galactocentric distance
23	e_R_{mean}	kpc	Error on mean galactrocentric distance
24	z_{max}	kpc	Distance from Galactic plane
25	e_z_{max}	kpc	Error on distance from Galactic plane
26	*e*	⋯	Orbital eccentricity
27	e_*e*	⋯	Error on orbital eccentricity
28	TD/D	⋯	Thick- to thin-disk probability ratio
29	[C/H]	dex	Carbon abundance
30	e_[C/H]	dex	Error on carbon abundance
71	[Zn I/H]	dex	Zinc abundance
72	e_[Zn I/H]	dex	Error on zinc abundance
73	[Fe I/H]	dex	Iron abundance
74	e_Fe I/H]	dex	Error on iron abundance
75	[Fe II/H]	dex	Ionized iron abundance
76	e_[Fe II/H]	dex	Error on ionized iron abundance
77	[alpha/Fe I]	dex	Averaged Mg I, Si I, Si II, Ca I, Ca II, Ti I, and Ti II to Fe I abundance ratio
78	e_[alpha/Fe I]	dex	Standard error of the mean on [α/Fe I]
79	Group	⋯	Chemical attribution to the Galactic subcomponent

(This table is available in its entirety in machine-readable form.)

ORCID iDs

G. Tautvaišienė https://orcid.org/0000-0001-7672-154X
Š. Mikolaitis https://orcid.org/0000-0002-1419-0517
A. Drazdauskas https://orcid.org/0000-0001-5145-254X
E. Stonkutė https://orcid.org/0000-0002-8028-8133
R. Minkevičiūtė https://orcid.org/0000-0001-6812-880X
E. Pakštienė https://orcid.org/0000-0002-3326-2918
H. Kjeldsen https://orcid.org/0000-0002-9037-0018
K. Brogaard https://orcid.org/0000-0003-2001-0276
Y. Chorniy https://orcid.org/0000-0001-8663-7077
C. von Essen https://orcid.org/0000-0002-6956-1725
F. Grundahl https://orcid.org/0000-0002-8736-1639
M. Ambrosch https://orcid.org/0000-0003-0804-6938
V. Bagdonas https://orcid.org/0000-0003-0848-1163
C. Viscasillas Vázquez https://orcid.org/0000-0001-5415-2796

References

Adibekyan, V. 2019, Geosc, 9, 105
Adibekyan, V., Dorn, C., Sousa, S. G., et al. 2021, Sci, 374, 330
Adibekyan, V., Gonçalves da Silva, H. M., Sousa, S. G., et al. 2017, Ap, 60, 325
Adibekyan, V., Santos, N. C., Figueira, P., et al. 2015, A&A, 581, L2
Adibekyan, V. Z., Santos, N. C., Sousa, S. G., et al. 2012a, A&A, 543, A89
Adibekyan, V. Z., Sousa, S. G., Santos, N. C., et al. 2012b, A&A, 545, A32
Agnew, M. T., Maddison, S. T., & Horner, J. 2018, MNRAS, 477, 3646
Alvarez, R., & Plez, B. 1998, A&A, 330, 1109
Asplund, M. 2004, MmSAI, 75, 300
Astropy Collaboration, Price-Whelan, A. M., Sipőcz, B. M., et al. 2018, AJ, 156, 123
Bailer-Jones, C. A. L., Rybizki, J., Fouesneau, M., Demleitner, M., & Andrae, R. 2021, AJ, 161, 147
Bang, T.-Y., Lee, B.-C., Jeong, G.-h., Han, I., & Park, M.-G. 2018, JKAS, 51, 17
Bashi, D., & Zucker, S. 2022, MNRAS, 510, 3449
Bedell, M., Bean, J. L., Meléndez, J., et al. 2018, ApJ, 865, 68
Benatti, S., Damasso, M., Desidera, S., et al. 2020, A&A, 639, A50
Bensby, T., Feltzing, S., & Lundström, I. 2003, A&A, 410, 527
Bensby, T., Feltzing, S., Lundström, I., & Ilyin, I. 2005, A&A, 433, 185
Bensby, T., Feltzing, S., & Oey, M. S. 2014, A&A, 562, A71
Bergemann, M., Hoppe, R., Semenova, E., et al. 2021, MNRAS, 508, 2236
Bitsch, B., & Battistini, C. 2020, A&A, 633, A10
Boisse, I., Pepe, F., Perrier, C., et al. 2012, A&A, 545, A55
Bovy, J. 2015, ApJS, 216, 29
Bovy, J., Allende Prieto, C., Beers, T. C., et al. 2012, ApJ, 759, 131
Bowler, B. P., Johnson, J. A., Marcy, G. W., et al. 2010, ApJ, 709, 396
Bressan, A., Marigo, P., Girardi, L., et al. 2012, MNRAS, 427, 127
Brooke, J. S. A., Bernath, P. F., Schmidt, T. W., & Bacskay, G. B. 2013, JQSRT, 124, 11
Burt, J., Feng, F., Holden, B., et al. 2021, AJ, 161, 10
Butler, R. P., Wright, J. T., Marcy, G. W., et al. 2006, ApJ, 646, 505
Clark, J. T., Clerté, M., Hinkel, N. R., et al. 2021, MNRAS, 504, 4968
Clegg, R. E. S., Lambert, D. L., & Tomkin, J. 1981, ApJ, 250, 262
Courcol, B., Bouchy, F., Pepe, F., et al. 2015, A&A, 581, A38
Cowley, C. R., Bord, D. J., & Yüce, K. 2021, AJ, 161, 142
Cridland, A. J., Eistrup, C., & van Dishoeck, E. F. 2019, A&A, 627, A127
Cutri, R. M., Wright, E. L., Conrow, T., et al. 2014, yCat, II/328, 1
da Silva, R., Milone, A. d. C., & Rocha-Pinto, H. J. 2015, A&A, 580, A24
Delgado Mena, E., Adibekyan, V., Santos, N. C., et al. 2021, A&A, 655, A99
Delgado Mena, E., Israelian, G., González Hernández, J. I., et al. 2010, ApJ, 725, 2349
Döllinger, M. P., Hatzes, A. P., Pasquini, L., et al. 2009, A&A, 499, 935
Dulick, M., Bauschlicher, C. W., Jr., Burrows, A., et al. 2003, ApJ, 594, 651
Endl, M., Brugamyer, E. J., Cochran, W. D., et al. 2016, ApJ, 818, 34
Fulton, B. J., Weiss, L. M., Sinukoff, E., et al. 2015, ApJ, 805, 175
Gaia Collaboration, Brown, A. G. A., Vallenari, A., et al. 2021, A&A, 649, A1
Gaia Collaboration, Prusti, T., de Bruijne, J. H. J., et al. 2016, A&A, 595, A1
Galland, F., Lagrange, A. M., Udry, S., et al. 2005, A&A, 444, L21
García Pérez, A. E., Allende Prieto, C., Holtzman, J. A., et al. 2016, AJ, 151, 144
González Hernández, J. I., Delgado-Mena, E., Sousa, S. G., et al. 2013, A&A, 552, A6
Grevesse, N., Asplund, M., & Sauval, A. J. 2007, SSRv, 130, 105
Gustafsson, B., Edvardsson, B., Eriksson, K., et al. 2008, A&A, 486, 951
Gustafsson, B., Karlsson, T., Olsson, E., Edvardsson, B., & Ryde, N. 1999, A&A, 342, 426
Hara, N. C., Bouchy, F., Stalport, M., et al. 2020, A&A, 636, L6
Hébrard, G., Arnold, L., Forveille, T., et al. 2016, A&A, 588, A145
Heiter, U., Lind, K., Asplund, M., et al. 2015, PhyS, 90, 054010
Mikolaitis, Š., Drazdauskas, A., Minkevičiūtė, R., et al. 2019, A&A, 628, A49
Mikolaitis, Š., Hill, V., Recio-Blanco, A., et al. 2014, A&A, 572, A33
Mikolaitis, Š., Tautvaišienė, G., Drazdauskas, A., et al. 2018, PASP, 130, 074202
Hinkel, N. R., Hartnett, H. E., & Young, P. A. 2020, ApJL, 900, L38
Hinkel, N. R., & Unterborn, C. T. 2018, ApJ, 853, 83
Jönsson, H., Holtzman, J. A., Allende Prieto, C., et al. 2020, AJ, 160, 120
Joshi, Y. C. 2007, MNRAS, 378, 768
Jurgenson, C., Fischer, D., McCracken, T., et al. 2016, JAI, 5, 1650003
Kervella, P., Arenou, F., Mignard, F., & Thévenin, F. 2019, A&A, 623, A72
Kokaia, G., Davies, M. B., & Mustill, A. J. 2020, MNRAS, 492, 352
Kolecki, J. R., & Wang, J. 2021, arXiv:2112.02031
Kurucz, R. 1993, Diatomic Molecular Data for Opacity Calculations: Kurucz CD-ROM No. 15 (Cambridge, MA: Smithsonian Astrophysical Observatory)
Lagarde, N., Reylé, C., Chiappini, C., et al. 2021, A&A, 654, A13
Lee, B. C., Han, I., Park, M. G., et al. 2014, A&A, 566, A67
Lindegren, L., Klioner, S. A., Hernández, J., et al. 2021, A&A, 649, A2
Liu, F., Bitsch, B., Asplund, M., et al. 2021, MNRAS, 508, 1227
Liu, F., Yong, D., Asplund, M., et al. 2020, MNRAS, 495, 3961
Luhn, J. K., Bastien, F. A., Wright, J. T., et al. 2019, AJ, 157, 149
Madhusudhan, N. 2019, ARA&A, 57, 617
Madhusudhan, N. 2021, ExoFrontiers: Big Questions in Exoplanetary Science (Bristol: IOP Publishing)
Masseron, T., Plez, B., Van Eck, S., et al. 2014, A&A, 571, A47
Meléndez, J., Asplund, M., Gustafsson, B., & Yong, D. 2009, ApJL, 704, L66
Mints, A., & Hekker, S. 2017, A&A, 604, A108
Mints, A., & Hekker, S. 2018, A&A, 618, A54
Mishenina, T., Basak, N., Adibekyan, V., Soubiran, C., & Kovtyukh, V. 2021, MNRAS, 504, 4252
Nibauer, J., Baxter, E. J., Jain, B., et al. 2021, AAS Meeting, 53, 332.04
Nordström, B., Mayor, M., Andersen, J., et al. 2004, A&A, 418, 989
Pereira, T. M. D., Kiselman, D., & Asplund, M. 2009, A&A, 507, 417
Ram, R. S., Brooke, J. S. A., Bernath, P. F., Sneden, C., & Lucatello, S. 2014, ApJS, 211, 5
Recio-Blanco, A., de Laverny, P., Kordopatis, G., et al. 2014, A&A, 567, A5
Ricker, G. R., Winn, J. N., Vanderspek, R., et al. 2015, JATIS, 1, 014003
Robertson, P., Endl, M., Cochran, W. D., et al. 2012, ApJ, 749, 39
Rosenthal, L. J., Fulton, B. J., Hirsch, L. A., et al. 2021, ApJS, 255, 8
Saffe, C., Jofré, E., Miquelarena, P., et al. 2019, A&A, 625, A39
Santos, N. C., Adibekyan, V., Figueira, P., et al. 2017, A&A, 603, A30
Sato, B., Omiya, M., Harakawa, H., et al. 2013, PASJ, 65, 85
Schneider, A. D., & Bitsch, B. 2021, A&A, 654, A71
Schönrich, R., Binney, J., & Dehnen, W. 2010, MNRAS, 403, 1829
Schulze, J. G., Wang, J., Johnson, J. A., et al. 2021, PSJ, 2, 113
Seabroke, G. M., Fabricius, C., Teyssier, D., et al. 2021, A&A, 653, A160
Sharma, S., Hayden, M. R., & Bland-Hawthorn, J. 2021, MNRAS, 507, 5882
Skrutskie, M. F., Cutri, R. M., Stiening, R., et al. 2006, AJ, 131, 1163
Smiljanic, R., Korn, A. J., Bergemann, M., et al. 2014, A&A, 570, A122
Sneden, C., Lucatello, S., Ram, R. S., Brooke, J. S. A., & Bernath, P. 2014, ApJS, 214, 26
Sneden, C. A. 1973, PhD thesis, Univ. of Texas at Austin
Soubiran, C., Le Campion, J.-F., Brouillet, N., & Chemin, L. 2016, A&A, 591, A118
Stassun, K. G., Collins, K. A., & Gaudi, B. S. 2017, AJ, 153, 136
Stetson, P. B., & Pancino, E. 2008, PASP, 120, 1332
Stonkutė, E., Chorniy, Y., Tautvaišienė, G., et al. 2020, AJ, 159, 90
Suárez-Andrés, L., Israelian, G., González Hernández, J. I., et al. 2016, A&A, 591, A69
Suárez-Andrés, L., Israelian, G., González Hernández, J. I., et al. 2017, A&A, 599, A96
Suárez-Andrés, L., Israelian, G., González Hernández, J. I., et al. 2018, A&A, 614, A84

Tautvaišienė, G., Edvardsson, B., Puzeras, E., Barisevičius, G., & Ilyin, I. 2010, MNRAS, 409, 1213
Tautvaišienė, G., Mikolaitis, Š., Drazdauskas, A., et al. 2020, ApJS, 248, 19
Thiabaud, A., Marboeuf, U., Alibert, Y., Leya, I., & Mezger, K. 2015, A&A, 580, A30
Tucci Maia, M., Meléndez, J., & Ramírez, I. 2014, ApJL, 790, L25
Turrini, D., Schisano, E., Fonte, S., et al. 2021, ApJ, 909, 40
Unterborn, C. T., & Panero, W. R. 2019, JGRE, 124, 1704
Wenger, M., Ochsenbein, F., Egret, D., et al. 2000, A&AS, 143, 9
Zhang, H.-P., Chen, Y.-Q., Zhao, G., et al. 2021, RAA, 21, 153